

Anand T. N. Kumar

Contents

22.1	Introduction	461
22.2	Theory	462
22.2.1	General forward problem statement	462
22.2.2	Frequency domain	463
22.2.3	Tomographic FLIM model	464
22.2.3.1	Frequency domain derivation of tomographic FLIM	464
22.2.3.2	Time domain derivation of tomographic FLIM	465
22.2.4	Conditions for recovery of <i>in vivo</i> fluorescence lifetimes	467
22.2.5	Inverse problem	468
22.3	Experimental methods	469
22.3.1	Imaging system	469
22.3.2	Impulse response and time origin	469
22.3.3	Multiexponential fits using global lifetime analysis	469
22.3.4	Single vs. multiexponential analysis	470
22.3.5	Noise considerations for lifetime multiplexing	471
22.4	<i>In vivo</i> tomographic FLIM	473
22.5	Conclusions and future outlook	474
	References	475

22.1 INTRODUCTION

Fluorescence lifetime imaging microscopy (FLIM) is a well-established technique (Bastiaens and Squire 1999; Berezovska et al. 2003; Selvin 2000; Vogel et al. 2006) that combines microscopic techniques with time-resolved detection to provide high-resolution lifetime images of thin tissue sections. This chapter concerns the *in vivo* time domain imaging of fluorescent contrast agents embedded in deep tissue. Optical molecular imaging is a rapidly growing field of interest (Bremer et al. 2003; Bugaj et al. 2001; Massoud and Gambhir 2003), with several contrast agents reported to date that cover the visible to the near infrared (NIR) spectral range. Although lifetime microscopy techniques are well established, whole body molecular imaging of lifetime contrast is relatively recent (Berezin et al. 2011; Bloch et al. 2005; Goiffon et al. 2009; Nothdurft et al. 2009; Raymond et al. 2010). One possible explanation for this discrepancy is the general concern among researchers about the viability of fluorescence lifetime as a useful marker for *in vivo* imaging, given that the fluorophore can undergo complex interactions with the biochemical environment *in vivo*, altering its photophysical properties in indeterminable ways. In fact, two distinct phenomena can alter the fluorescence lifetimes as measured on the surface of a living subject. The first is the interaction of the fluorophore with the biological environment (e.g., pH, viscosity, and protein binding). The effect of tissue environment on the lifetime can be characterized in advance using careful control measurements (Raymond et al. 2010). The second phenomenon is the interaction of light with tissue, which can also

indirectly affect the temporal response of the fluorophore as measured on the surface. This chapter is mainly concerned with the second phenomenon, namely, the influence of tissue scattering and absorption on the lifetime of fluorophores embedded in biological tissue. The details of this influence are incorporated through differential equations that describe light propagation in scattering media. We will, in particular, derive a tomographic FLIM model, which is valid under a widely applicable condition, namely, that the fluorescence lifetime is longer than the intrinsic diffusive timescales in the medium. Under this “FLIM condition,” the temporal decay of fluorescence from deep tissue can be directly used to recover both the *in vivo* lifetimes and their corresponding yield distributions. Further, this model naturally leads to an elegant algorithm for tomographic FLIM, which allows the complete 3D separation of multiple lifetimes present within biological tissue. We will also discuss experimental aspects of performing tomographic FLIM in turbid media and present *in vivo* results using organ-specific contrast agents.

22.2 THEORY

22.2.1 GENERAL FORWARD PROBLEM STATEMENT

A typical tomography measurement involves optical sources and detectors placed on the boundary of the imaging specimen. The detected fluorescence can be described as a sequential propagation of the excitation light from the source(s) to the fluorophore, fluorophore emission, and propagation of the emission field from the fluorophore to the detector. This is described using coupled equations for light transport at the excitation and emission wavelengths. Let the source and detector locations be \mathbf{r}_s and \mathbf{r}_d . Let $\eta(\mathbf{r})$ be the yield distribution (product of the quantum yield Q , concentration, and extinction coefficient) of the fluorophore, with \mathbf{r} denoting the location of a point within the medium (voxel). The expression for the detected fluorescence in the time domain (TD) can then be written as a double convolution of the excitation ($G^x(\mathbf{r}, \mathbf{r}_s, t)$) and emission ($G^m(\mathbf{r}_d, \mathbf{r}, t)$) Green's functions (GFs) with the fluorescence decay term ($e^{-t/\tau(\mathbf{r})}$) (additional scaling factors are necessary when considering experimental data, including the source and detector coefficients, geometrical factors, and fluorescence filter attenuation):

$$U(\mathbf{r}_s, \mathbf{r}_d, t) = \int_{\Omega} d^3r W(\mathbf{r}_s, \mathbf{r}_d, \mathbf{r}, t) \eta(\mathbf{r}), \quad (22.1)$$

where the weight function (also called the “sensitivity” function) is given by

$$W(\mathbf{r}_s, \mathbf{r}_d, \mathbf{r}, t) = \int_0^t dt' \int_0^{t'} dt'' G^m(\mathbf{r}_d, \mathbf{r}, t - t') e^{-\Gamma(\mathbf{r})(t' - t'')} G^x(\mathbf{r}, \mathbf{r}_s, t''), \quad (22.2)$$

where $\tau(\mathbf{r}) = 1/\Gamma(\mathbf{r})$ is the fluorescence lifetime distribution. The above equation ignores re-emission of the fluorescence by the fluorophore, an assumption used widely in applications of tomographic fluorescence imaging and also termed the “Born approximation.” Besides this approximation, the accuracy of Equation 22.1 depends on the level of approximation used for estimating the GFs, which depend on the intrinsic tissue optical properties, namely, absorption ($\mu_a^x(\mathbf{r}), \mu_a^m(\mathbf{r})$) and scattering ($\mu_s^x(\mathbf{r}), \mu_s^m(\mathbf{r})$) distributions at the excitation (λ_x) and emission (λ_m) wavelengths, in addition to the tissue anisotropy factor g . In general, the absorption and scattering are heterogeneous and include tissue components (such as water, melanin, and blood) and the absorption of the fluorophore (at both λ_x and λ_m). Generally, all the parameters, $\eta(\mathbf{r})$, $\tau(\mathbf{r})$, $\mu_a^{(x,m)}(\mathbf{r}), \mu_s^{(x,m)}(\mathbf{r})$ are unknown. A common starting point is the homogeneous approximation where the optical properties are assumed uniform throughout and fluorophore absorption is ignored for evaluating the GFs. In this case, the GFs in Equation 22.2 are the solutions to the homogeneous diffusion or transport equations. Note that $\mu_a^{x,m}$ and $\mu_s^{x,m}$ can, in practice, be determined independently using two separate “excitation” measurements at wavelengths λ_x and λ_m . In this case, Equation 22.2 can provide a highly accurate description of time-resolved fluorescence in turbid media. With $\mu_a^{x,m}$ and $\mu_s^{x,m}$ known, the GFs can be calculated using either the diffusion approximation or the radiative transport equation.

Evaluation of the sensitivity (Equation 22.2) can become computationally intractable for multiple source–detector (S–D) pairs ($\sim 10^2$), medium voxels ($\sim 10^4$), and time points ($\sim 10^3$). One simplifying approach is to solve Equation 22.2 in the frequency (Fourier) domain (FD), since the double convolution then simplifies to a product for each frequency. While convenient in some scenarios (Nothdurft et al. 2009; Soloviev et al. 2007), this approach has the limitation that the Fourier transform is nontrivial for multiexponential decays, and multiple frequencies are required to reliably extract multiple lifetimes or complex decay profiles. Existing TD approaches to solve Equation 22.2 are overly simplistic (such as assuming point fluorophores in an infinite homogeneous medium; Hall et al. 2004), while the general formalism is quite intractable (Arridge and Schotland 2009). In what follows, we will take an approach to solve Equation 22.1 that is motivated by a practical observation, namely, that typical fluorescence lifetimes (τ) of fluorophores from the visible to NIR wavelengths are longer than the timescales for intrinsic diffusive relaxation in small volumes, τ_D (which is shorter than the absorption timescale $\tau_a = (v\mu_a)^{-1}$; Haselgrove et al. 1992). We will make more precise definition of τ_D in Section 22.2.4. Under the approximation that $\tau > \tau_D$, it will be shown that Equations 22.1 and 22.2 can be cast into an elegant and rigorous formalism for inverting multiple lifetimes within turbid media (Kumar et al. 2005) that is analogous to the multiexponential model in FLIM. We will derive this “tomographic-FLIM” approach both in the frequency domain, using complex integration, and in time domain using Equation 22.2. Before proceeding, it is convenient to recast Equations 22.1 and 22.2 in the following way using the commutativity of the convolution:

$$U(\mathbf{r}, \mathbf{r}_d, t) = \int_{\Omega} d^3r \int_0^t dt' W^B(\mathbf{r}, \mathbf{r}_d, \mathbf{r}, t') \left[\sum_n e^{-\Gamma_n(t-t')} \eta_n(\mathbf{r}) \right], \quad (22.3)$$

where we have defined a “background” weight function as

$$W^B(\mathbf{r}, \mathbf{r}_d, \mathbf{r}, t') = \int_0^{t'} dt'' G^x(\mathbf{r}, \mathbf{r}, t' - t'') G^m(\mathbf{r}, \mathbf{r}_d, t''), \quad (22.4)$$

and $\Gamma_n = 1/\tau_n$ are discretized values of the *in vivo* lifetime distribution with corresponding yield distributions $\eta_n(\mathbf{r})$. In other words, each lifetime has a distinct yield distribution. We will see below that the $\eta_n(\mathbf{r})$'s can be separately reconstructed from analyzing the TD data.

22.2.2 FREQUENCY DOMAIN

One way to analyze the TD forward problem is to Fourier-transform the data. In the frequency domain, the double convolution in the integrand of Equation 22.4 reduces to a simple product:

$$U(\mathbf{r}, \mathbf{r}_d, t) = \int_{\Omega} d^3r \int_{-\infty}^{\infty} d\omega e^{-i\omega t} \tilde{W}^B(\mathbf{r}, \mathbf{r}_d, \mathbf{r}, \omega) \underbrace{\left[\sum_n \frac{\tau_n \eta_n(\mathbf{r})}{(1 - i\omega\tau_n)} \right]}_{F(\mathbf{r}, \omega)}. \quad (22.5)$$

where

$$\tilde{W}^B(\mathbf{r}, \mathbf{r}_d, \mathbf{r}, \omega) = \tilde{G}^x(\mathbf{r}, \mathbf{r}, \omega) \tilde{G}^m(\mathbf{r}_d, \mathbf{r}, \omega) \quad (22.6)$$

is the FD sensitivity obtained as a Fourier transform of the TD sensitivity (Equation 22.4), with ω as the modulation frequency. The standard FD approach (see, for example, Chapter 13) is to reconstruct the spatial distribution of $F(\mathbf{r}, \omega)$ (quantity within the square brackets in Equation 22.5) from the FD measurements at a given frequency ω . The lifetime and yield distributions are obtained as the phase and the

real part of $F(\mathbf{r}, \omega)$, respectively. As is clear from Equation 22.5, the TD data provide multiple frequencies. Handling multiple frequencies with the above forward problem becomes complicated since $F(\mathbf{r}, \omega)$ inseparably involves both a measurement parameter ω and the unknown lifetime $\tau(\mathbf{r})$. This necessitates a nonlinear approach as described, for example, in Milstein et al. (2003). However, it has also been shown that multiple frequencies do not necessarily improve the quality of the reconstruction (Milstein et al. 2004), with the number of useful frequencies restricted to the first three or four frequency components from zero.

22.2.3 TOMOGRAPHIC FLIM MODEL

The TD forward problem in Equations 22.3 and 22.4 can be reduced to a sum of exponential decays, analogous to the signal in microscopic FLIM (Bastiaens and Squire 1999), the difference being that the amplitude coefficients of the lifetimes will now correspond to a measurement set for tomographic reconstructions, while in microscopy, they directly relate to the amplitude of the lifetime component in a particular tissue location. We will prove this result using two different methods, one using the FD form in Equation 22.5 and the other directly from the general TD forward problem, viz., Equations 22.3 and 22.4. The result derived using the direct TD approach is applicable to the entire TD fluorescence signal, while the FD approach is applicable only to the asymptotic or long-time portion of the TD fluorescence. The TD approach results in a tomographic FLIM model that clearly elucidates the individual contributions of the diffusive background and fluorescence decay to the measured TD fluorescence signal. We will also discuss the conditions when the tomographic FLIM model is valid.

22.2.3.1 Frequency domain derivation of tomographic FLIM

We apply contour integration (from complex analysis; Matthews and Walker 1970) to solve the FD integral in Equation 22.5. Without loss of generality, we consider an infinite homogeneous medium (the results will, however, be shown later to be valid for bounded heterogeneous media) and examine the analytic nature, in the complex variable sense, of the integrand of Equation 22.5. The homogeneous GFs are $\tilde{G}^{(x,m)}(\mathbf{r}_1, \mathbf{r}_2, \omega) = \exp(ik^{(x,m)}\rho_{12})/4\pi D^{(x,m)}$, where $\rho_{12} = |\mathbf{r}_1 - \mathbf{r}_2|$, $k^{(x,m)} = [(-v\mu_a^{(x,m)} + i\omega)/D^{(x,m)}]^{1/2}$, $D^{(x,m)} = v/3\mu_s^{(x,m)}$ is the diffusion coefficient, and v is the velocity of light in the medium. It is evident that the integrand in Equation 22.1 possesses simple pole singularities distributed along the negative imaginary axis at $\omega_n = -i\Gamma_n$ (see Figure 22.1) due to the fluorescence decay term, $F(\mathbf{r}, \omega)$. In addition, the homogeneous GF and its spatial derivatives are bi-valued owing to the square root in k , implying branch points (Matthews and Walker 1970) in the lower half plane at $\omega = -iv\mu_a^{(x,m)}$. To evaluate U (Equation 22.5), we choose a contour (C) shown in the complex “ ω -plane” in Figure 22.1 and apply Cauchy’s integral theorem

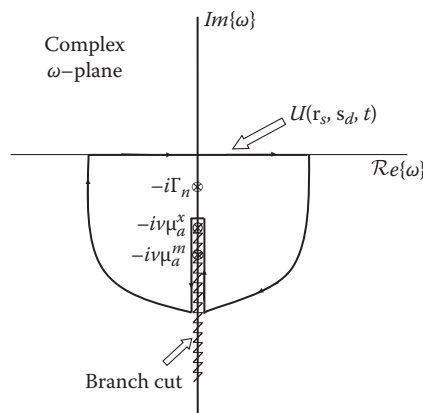


Figure 22.1 Complex ω -plane structure of the integrand of Equation 22.5 for a homogeneous diffuse medium, showing the simple pole singularities at $\omega = -i\Gamma_n$ and the branch points at $\omega = -iv\mu_a^{(x,m)}$. It is assumed that $\Gamma_n < v\mu_a^{(x,m)}$. Also shown is the contour for calculating Equation 22.5 using Cauchy’s theorem. The integral of Equation 22.5 corresponds to the contribution of the real- ω axis extended from $-\infty$ to ∞ .

(Matthews and Walker 1970), whence U separates into a sum of two terms, the first term arising from the residue at the simple poles at $-i\Gamma_n$ (which will lead to a sum of pure fluorescence decays) and the second term arising from the integration on either side of the branch cut (Matthews and Walker 1970) along the branch points in the lower imaginary axis (which will lead to a fluorescent diffuse photon density wave):

$$U(\mathbf{r}_s, \mathbf{r}_d, t) = \sum_n a_{Fn}(\mathbf{r}_s, \mathbf{r}_d) e^{-\Gamma_n t} + a_D(\mathbf{r}_s, \mathbf{r}_d, t) e^{-\nu\mu_a t} \quad (22.7)$$

where a_{Fn} denote the decay amplitudes of the fluorophore with lifetime $\tau_n = 1/\Gamma_n$ and are readily obtained as the residue (Matthews & Walker 1970) of the integrand in Equation 22.5 at the simple poles at $-i\Gamma_n$. This leads to the following linear inverse problem for the yield distribution $\eta_n(\mathbf{r})$ of the n th fluorophore:

$$a_{Fn}(\mathbf{r}_s, \mathbf{r}_d) = \int_V d^3r \tilde{W}_n^B(\mathbf{r}_s, \mathbf{r}_d, \mathbf{r}, -i\Gamma_n) \eta_n(\mathbf{r}). \quad (22.8)$$

with a weight matrix \tilde{W}_n^B for inverting the n th lifetime component τ_n simply given by the FD weight matrix (Equation 22.6) but evaluated at an imaginary frequency of $\omega = -i\Gamma_n$. For this imaginary frequency, we have

$$(k^{(x,m)})^2 = \frac{(-\nu\mu_a^{(x,m)} + \Gamma_n)}{D^{(x,m)}} = \frac{-\nu(\mu_a^{(x,m)} - \Gamma_n/\nu)}{D^{(x,m)}} = \frac{-\nu\mu_{an}'^{(x,m)}}{D^{(x,m)}} \quad (22.9)$$

where we have defined a “reduced” absorption, $\mu_{an}' = \mu_a - \Gamma_n/\nu$. But Equation 22.9 is identical to the definition of k for the CW diffusion (Helmholtz) equation, showing that \tilde{W}_n^B are sensitivity functions for the CW diffusion equation with a reduced absorption. If we assume that $\Gamma_n < \nu\mu_a^{(x,m)}$, that is, $\tau_n > 1/\nu\mu_a^{(x,m)}$, it is clear that the first term in Equation 22.7 dominates the long-time behavior of the net fluorescence signal. We call this region the asymptotic region, where $t > \tau_a$. We thus see that the TD fluorescence forward problem reduces “asymptotically” to multiple CW forward problems with a separate effective absorption of μ_{an}' for each lifetime. As can be checked easily, $\tau_a < 0.5$ ns for $\mu_a > 0.1/\text{cm}$ (typical value for biological tissue), which means that the asymptotic TD decay is dominated by the fluorescence lifetimes that are longer than a few subnanoseconds. We will, in fact, see in the next section that the diffusive timescale from a finite volume is even shorter than τ_a . It is also possible to evaluate the second term of Equation 22.7 as the contribution of the integration on either side of the branch cuts. But this signal is negligible from the point of view of fluorescence lifetime, and we therefore do not derive it here. We will show in the next section that the multiexponential form of the first term of Equation 22.7 also holds for the entire temporal response but with a time-dependent decay amplitude.

Although the above results were derived assuming a homogeneous infinite medium, a general solution for the inhomogeneous diffusion equation in a bounded volume may be written in terms of the homogeneous GF and its normal derivatives at the boundary (Barton 1989). It is thus plausible to assert that the complex plane structure in Figure 22.1 also applies to arbitrary heterogeneous media. This implies that Equation 22.8 can be generalized to arbitrary media by simply substituting the GF solutions of the heterogeneous diffusion equation with finite boundary models. In the next section, we will indeed derive a general time-dependent, reduced-absorption decay amplitude that smoothly goes over to Equation 22.8 in the asymptotic limit and is valid for bounded heterogeneous media. The definition of the asymptotic region, when the fluorescence decay is dominant, will also be made more precise.

22.2.3.2 Time domain derivation of tomographic FLIM

Consider the full TD forward problem given in Equations 22.3 and 22.4. We start with the following general result (Kumar et al. 2006) for the GF for the heterogeneous transport equation (Arridge 1999; Chandrasekhar 1960):

$$G^{(x,m)}(\mathbf{r}, t) = G^{(x,m)}(\mathbf{r}, t) e^{-\nu\mu_a^{(x,m)}(\mathbf{r})t}, \quad (22.10)$$

where the functions $G^{(x,m)}$ are dependent only on the *gradient* of the absorption coefficient, $\mu_a^{(x,m)}(\mathbf{r})$, and independent of $\mu_a^{(x,m)}(\mathbf{r})$ itself (note that this result is a generalization of Equation 2 in Durduran et al. 1997, which is for a homogeneous medium). Thus, the functions $G^{(x,m)}$ are invariant to constant shifts in the absorption. This means that under the long lifetime condition, $\Gamma_n < \nu\mu_a^{(x,m)}(\mathbf{r})$, $\forall \mathbf{r} \in \Omega$, the exponential factor in the integrand of Equation 22.3 can be absorbed into the GFs as follows: since $e^{\Gamma_n t'} = e^{\Gamma_n(t'-t'')}e^{\Gamma_n t''}$, we can write, using Equation 22.4,

$$W^B(\mathbf{r}_s, \mathbf{r}_d, \mathbf{r}, t') e^{\Gamma_n t'} = \int_0^{t'} dt'' \left[G^x(\mathbf{r}_s, \mathbf{r}, t' - t'') e^{\Gamma_n(t'-t'')} \right] \left[G^m(\mathbf{r}, \mathbf{r}_d, t'') e^{\Gamma_n t''} \right].$$

Using Equation 22.10 and the property that $G^{(x,m)}$ are unaffected by a constant shift in the absorption, and defining a heterogeneous reduced absorption $\mu_a'^{(x,m)}(\mathbf{r}) = \mu_a^{(x,m)}(\mathbf{r}) - \Gamma_n/\nu$, the right-hand side of the above equation becomes

$$\begin{aligned} & \int_0^{t'} dt'' \left[G^x(\mathbf{r}_s, \mathbf{r}, t' - t'') e^{-\nu\mu_a'^{(x,m)}(\mathbf{r})(t'-t'')} \right] \left[G^m(\mathbf{r}, \mathbf{r}_d, t'') e^{-\nu\mu_a'^{(x,m)}(\mathbf{r})t''} \right] \\ &= \int_0^{t'} dt'' G_n^x(\mathbf{r}_s, \mathbf{r}, t' - t'') G_n^m(\mathbf{r}, \mathbf{r}_d, t'') \\ &= W_n^B(\mathbf{r}_s, \mathbf{r}_d, \mathbf{r}, t'). \end{aligned} \quad (22.11)$$

Here we have defined a TD sensitivity W_n^B (counterpart of the FD sensitivity \tilde{W}_n^B in Equation 22.8), which is evaluated as in Equation 22.4 but using transport GFs, $G_n^{(x,m)}$, that are evaluated with a reduced absorption, $\mu_a'^{(x,m)}$. We finally substitute Equation 22.11 into Equation 22.3 and get the following form for the TD fluorescence signal when $\Gamma_n < \nu\mu_a^{(x,m)}(\mathbf{r})$, $\forall \mathbf{r} \in \Omega$:

$$U(\mathbf{r}_s, \mathbf{r}_d, t) = \sum_n e^{-\Gamma_n t} \int d^3 r \left[\int_0^t dt' W_n^B(\mathbf{r}_s, \mathbf{r}_d, \mathbf{r}, t') \right] \eta_n(\mathbf{r}). \quad (22.12)$$

The above equation reduces to an elegant multiexponential form:

$$U(\mathbf{r}_s, \mathbf{r}_d, t) = \sum_n A_n(\mathbf{r}_s, \mathbf{r}_d, t) e^{-\Gamma_n t} \quad (22.13)$$

but with time-dependent decay amplitudes A_n , given by

$$A_n(\mathbf{r}_s, \mathbf{r}_d, t) = \int d^3 r \left[\int_0^t dt' W_n^B(\mathbf{r}_s, \mathbf{r}_d, \mathbf{r}, t') \right] \eta_n(\mathbf{r}). \quad (22.14)$$

The time dependence of the decay amplitudes A_n reflects the evolution of the background diffusive response. In Figure 22.2, the simulated temporal evolution of $A(t)$ is shown for diffusive slabs of thicknesses 2 and 10 cm, with a 2 mm³ fluorophore inclusion of 1 ns lifetime embedded at the center of the slab. The net fluorescence signal calculated using tomo-FLIM model in Equations 22.13 and 22.14 is compared with the fluorescence signal computed directly using Equations 22.3 and 22.4 and confirms the accuracy of tomo-FLIM model over a wide range of medium thicknesses that includes small animal to human imaging applications. Note that $A(t)$ rapidly reaches a constant value, beyond which the temporal evolution of $U(\mathbf{r}_s, \mathbf{r}_d, t)$ is purely exponential. Indeed, it is clear that Equation 22.14 approaches Equation 22.8 in

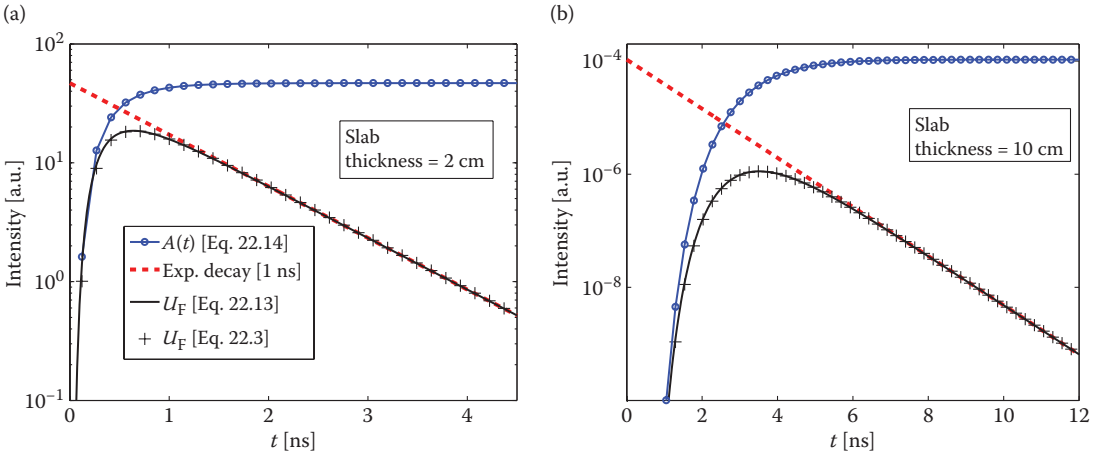


Figure 22.2 Simulations to elucidate the diffuse and pure fluorescent decay components as revealed by the time domain fluorescence model presented in Equation 22.13. The medium was an infinite slab of thickness 2 cm (a) and 10 cm (b), with optical properties $\mu_s^x = \mu_s^m = 10/\text{cm}$, $\mu_a^x = \mu_a^m = 0.1/\text{cm}$. The fluorescence signal was calculated for a single source detector pair, with a small fluorescent inclusion at the center. The signal calculated using the conventional approach in Equation 22.3 (+ symbol) is compared with that calculated using an effective-absorption-based model, viz., Equation 22.13 (solid black line). The decay amplitude, $A(t)$ (dotted blue line) and pure fluorescence decay (dashed red line) are also delineated for both cases.

the asymptotic limit, since \tilde{W}_n^B is just the CW (or time integrated) version of W_n^B , so that $A_n(\mathbf{r}_s, \mathbf{r}_d, t) \rightarrow a_n(\mathbf{r}_s, \mathbf{r}_d)$ in the asymptotic limit. The time constant for the rise of $A(t)$ toward a_n (see the next section) will depend on the intrinsic tissue absorption, scattering, and size of the imaging volume. We define the “asymptotic regime” for times when the time average of W_n^B (which is the integrand of $A(t)$) in Equation 22.14 will become nearly time independent and approach the CW sensitivity function, which we denote by $\bar{W}_n^B (= \tilde{W}_n^B(-i\Gamma_n))$. We thus have

$$U(\mathbf{r}_s, \mathbf{r}_d, t) \xrightarrow{t > \tau_D} \sum_n e^{-\Gamma_n t} \underbrace{\int d^3r \bar{W}_n^B(\mathbf{r}_s, \mathbf{r}_d, \mathbf{r}) \eta_n(\mathbf{r})}_{a_{Fn}(\mathbf{r}_s, \mathbf{r}_d)}. \quad (22.15)$$

In other words, Equation 22.14 approaches Equation 22.8 in the asymptotic limit. Equation 22.13 therefore constitutes a generalized multiexponential forward problem for tomographic FLIM that includes both early and late arriving photons and is rigorous within the radiative transport model of photon propagation in turbid media.

22.2.4 CONDITIONS FOR RECOVERY OF *IN VIVO* FLUORESCENCE LIFETIMES

The natural question in the mind of any researcher interested in whole-body FLIM is, under what conditions can intrinsic fluorescence lifetimes reliably be measured on the surface of a living subject? As mentioned in Section 22.1, the intrinsic fluorescence lifetime of a fluorophore can be altered *in vivo* either because of (a) the tissue environment or (b) light scattering and absorption in tissue. This chapter concerns the latter phenomenon, with the understanding that the “intrinsic” lifetime refers to the lifetime of the fluorophore in the biological environment, which can be separately characterized in advance (Raymond et al. 2010). There are two timescales involved. Firstly, $\tau_a = 1/\nu\mu_a$ is the asymptotic decay time of the intrinsic diffuse temporal response in the limit of homogenous semi-infinite media (Patterson et al. 1989). The second is the actual decay time, τ_D , for the intrinsic photon diffusion in a finite-sized object (which is also related to the rise-time constant of the TD decay amplitude, $A(t)$; Figure 22.2). The time constant

τ_D is always shorter than τ_a due to the presence of boundaries (Haselgrove et al. 1992; Patterson et al. 1989), that is, $\tau_D < \tau_a$ (a numerical evaluation of τ_D for a range of tissue optical properties can be found in Kumar et al. 2005). Since the net fluorescence signal is a convolution of the pure fluorescence decay with intrinsic diffusive response, the condition $\tau_n > \tau_a$ guarantees that the intrinsic lifetimes within tissue can be measured asymptotically from surface fluorescence decays,* irrespective of scattering and medium size. Furthermore, the tomo-FLIM model presented in Equation 22.13 is valid.

The condition $\tau_n > \tau_a$ is easily satisfied for approximately nanosecond lifetime fluorophores in biomedical applications ($\mu_a = 0.1/\text{cm}$ corresponds to $\tau_a = 0.5$ ns). The simple rule that $\tau_n > \tau_a$ with τ_a denoting the average absorption for a heterogeneous medium dictates the condition for measuring intrinsic lifetimes from whole animals and for the applicability of the tomographic FLIM model. For heterogeneous media, care should be exercised in using the reduced absorption model in Equation 22.13 in avoiding regions with a negative value for μ'_a . The exact influence of low absorption regions on the reduced absorption model will be studied in future work.

22.2.5 INVERSE PROBLEM

The previous sections were concerned with the forward problem for time domain fluorescence tomography. The inverse problem consists of determining the fluorescence yield and lifetime distributions (and the background tissue optical properties, if they are not known) from measured fluorescence and excitation data. In the tomo-FLIM approach, the lifetimes are first obtained as discrete values by fitting the decay (asymptotic) portion of the TD data (which constitutes an inversion problem itself, via the inverse Laplace transform; Kumar et al. 2001). We only need to determine the fluorescence yield distributions, $\eta(\mathbf{r})$. We refer the reader to standard texts for a general treatment of linear inverse problems (Bertero and Boccacci 1998). Here, we present a simple approach that illustrates what is involved. Equation 22.8 is in the form of an underdetermined problem of the form $y = Wx$, where W is a general sensitivity matrix. The pseudo-inverse W_s^{-1} defined by $x = W_s^{-1}y$ is given as

$$W_s^{-1} = L^{-1}\tilde{W}^T (\tilde{W}\tilde{W}^T + \alpha\lambda I)^{-1}, \quad (22.16)$$

where $\tilde{W} = WL^{-1}$, with L as a diagonal matrix whose diagonal elements are $\sqrt{\text{diag}(W^T W)}$, λ is the regularization parameter, and $\alpha = (\max(\text{diag}(\tilde{W}\tilde{W}^T)))$. Note that since $(W^T W)_{ij} = \sum_l W_{li} W_{lj}$, we have

$$L_{ii} = \sqrt{(W^T W)_{ii}} = \sqrt{\sum_l W_{li}^2}. \quad (22.17)$$

Thus, the diagonal elements of L are the column norms of the sensitivity function W or the net sensitivity at each voxel summed over all measurement pairs. The normalization by L therefore has the effect of annulling the strong spatial variations in the sensitivity function. In order to reduce the computational time for evaluating the inverse in Equation 22.16 for multiple regularization parameters, an SVD analysis can be employed. Writing $\tilde{W} = USV^T$, it can be readily shown that

$$x = L^{-1}VS(S^2 + \alpha\lambda I)^{-1}U^T y. \quad (22.18)$$

* Note that for heterogeneous media, it is known that the intrinsic diffusive decay time τ_a is relatively constant on the measurement surface (Haselgrove et al. 1992), so that we can use the average or "baseline" absorption of the tissue medium to estimate τ_a .

22.3 EXPERIMENTAL METHODS

22.3.1 IMAGING SYSTEM

The imaging system for tomographic FLIM essentially consists of a light source, a fiber to deliver the light to the surface of the animal or subject, and a detection system that can be either wide-field-based using a CCD camera or point-based using fibers. In order to provide nanosecond time resolution, either a gated camera (Nothdurft et al. 2009; Raymond et al. 2010) or time-correlated single-photon counting (TCSPC) (Bloch et al. 2005) is used. These experimental methods are discussed in detail in Chapters 6 and 9. A detailed description of a small animal TD fluorescence tomography system can be found in Kumar et al. (2008b). Below we briefly discuss some experimental techniques specific to wide-field detected tomographic FLIM.

22.3.2 IMPULSE RESPONSE AND TIME ORIGIN

An important parameter for tomographic FLIM is the system impulse response function (IRF) as well as an accurate estimate t_0 , which is the time when the excitation pulse is incident on the surface of the imaging medium (we have set $t_0 = 0$ in the derivations above). A correct estimate of the time origin t_0 ensures that the relative amplitudes of the multiple lifetime components are correct (Kumar et al. 2006), and is crucial for estimating the optical properties using TD data, as well as for fluorescence reconstructions using the early time gates (Niedre et al. 2008). An advantage of noncontact detection is that t_0 can be estimated from the IRF, which can, in turn, be measured directly from the source illumination. This is possible since the position of the CCD camera (i.e., the detectors) is unchanged before and after the sample is placed on the imaging plate, unlike in contact geometries with fiber-based detection. Note that the time t_0 measured from the IRF includes the time for free space propagation of light from the source to the camera. However, the propagation time for the fluorescence emitted from the imaging surface to the detector will be slightly shorter than t_0 , due to the finite thickness of the mouse. Before analyzing the fluorescence data, t_0 should therefore be offset by the sample thickness, for example, ≈ 50 ps for a mouse of thickness 2 cm. The measured IRF can be directly forward-convolved into the model before tomographic inversion. This procedure is superior to a deconvolution of the IRF from the raw fluorescence data, which is a highly ill-posed problem. For the asymptotic reconstructions, the effect of the IRF on the forward model can be calculated analytically for a square IRF. Using Equation 22.15, the influence of a square IRF of width T is given as

$$\begin{aligned} \lim_{t > \tau_D} U_T(\mathbf{r}_s, \mathbf{r}_d, t) &= \int_t^{t+T} \lim_{t > \tau_D} U(\mathbf{r}_s, \mathbf{r}_d, t) \\ &= \sum_n \tau_n (1 - e^{-T/\tau_n}) a_n(\mathbf{r}_s, \mathbf{r}_d) e^{-\Gamma_n t}. \end{aligned} \quad (22.19)$$

Thus, the effect of the system IRF on the measured decay amplitudes is a scaling factor that depends on the lifetime and the width of the IRF. The decay amplitudes a_{Fn} need to be scaled by the coefficient $\tau_n (1 - e^{-T/\tau_n})$ before being inverted using Equation 22.18. This scaling factor is essentially the result of a partial averaging of the exponential decay in Equation 22.19 and approaches the CW signal in the limit $T \rightarrow \infty$.

22.3.3 MULTIEXPONENTIAL FITS USING GLOBAL LIFETIME ANALYSIS

An important step in the asymptotic approach is the extraction of the decay amplitudes for all the lifetimes present in the medium. The recovery of lifetimes and decay amplitudes from multiexponential fits to decay data is a nonlinear problem, which is further complicated by the presence of noise. However, the tomographic-FLIM model (Equation 22.8) allows for a significant simplification of the fitting process. Since the set of discretized lifetime components, τ_n , are independent of the measurement locations (i.e., the S–D coordinates $(\mathbf{r}_s, \mathbf{r}_d)$), the multiexponential analysis can be performed in two stages. First, the total fluorescence

decay is calculated as a sum over all S–D pairs to obtain a high signal-to-noise ratio temporal data set. This “global” signal is composed of all the lifetime components present in the system and allows a more robust determination of the lifetimes through a nonlinear analysis. In the second step, the lifetimes determined from the S–D-integrated decays are used in a *linear* fit of the decays for each individual S–D pair. Besides improving the robustness of the fitting procedure for the lifetimes and decay amplitudes, the global analysis is computationally much less cumbersome than performing a nonlinear fit for every S–D measurement. Chapters 10 through 12 present a detailed review of existing methods for FLIM data analysis, which can be directly incorporated for tomographic FLIM in turbid media using Equation 22.8.

22.3.4 SINGLE VS. MULTIEXPONENTIAL ANALYSIS

When two or more fluorophores are present simultaneously in an animal, the measured fluorescence is a sum of photons from the respective fluorophores. Monoexponential analysis of a mixed signal provides an average lifetime for each detector or pixel, but can be misleading given the contribution of the fluorophores at different concentrations and quantum efficiencies. In contrast, a multiexponential analysis based on expected lifetime components can produce a quantitative measure of multiple fluorophores. Moreover, a monoexponential analysis does not exploit the full power of lifetime-based tomographic separability as afforded by Equation 22.8. As an example, consider multiplexing Osteosense 750 (PerkinElmer), a bone-targeted NIR probe, with X-Sight 761 (Kodak), a NIR probe that remains in the blood stream and accumulates slowly in the liver. When just Osteosense 750 is present in the animal, the monoexponential lifetime map exhibits a narrow lifetime distribution with mean $\tau = 835$ ps (Figure 22.3b). Administration

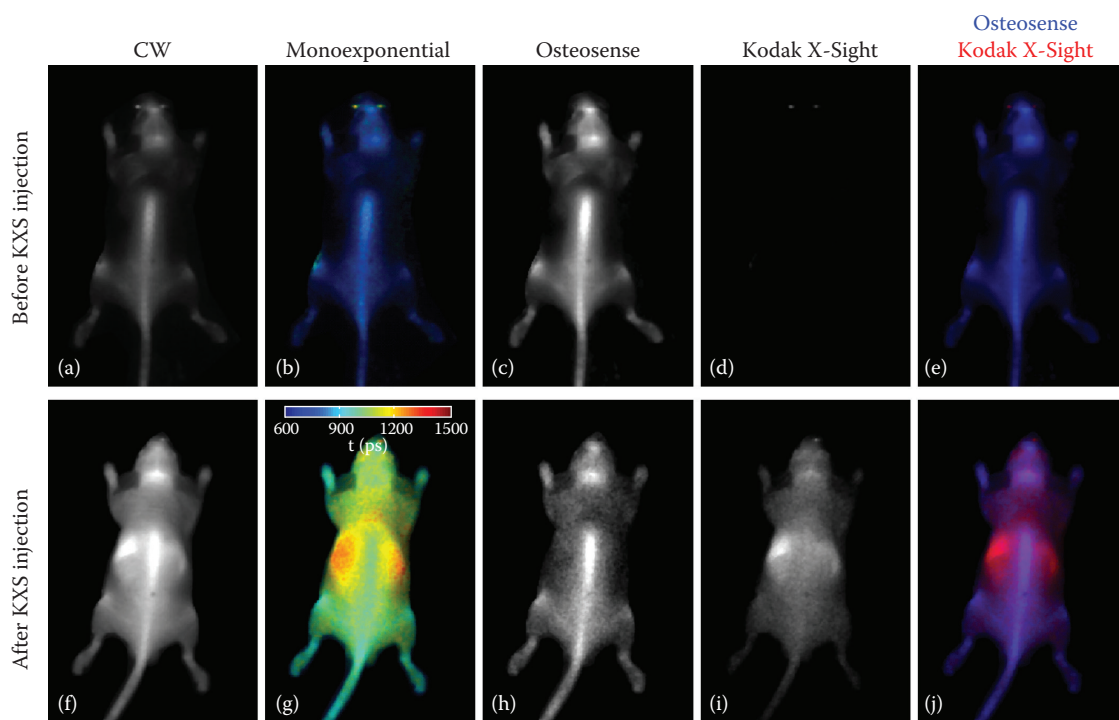


Figure 22.3 Planar FLIM of Osteosense 750 and Kodak X-Sight 761. A nude mouse received 2 nmol Osteosense 24 h prior to imaging; planar fluorescence time-resolved images were collected immediately before (a–e) and after (f–j) administration of Kodak X-Sight 761 (3 nmol). Image pixels were fit for the amplitude and lifetime of a monoexponential function or were fit with a linear biexponential function. (a, f) Continuous wave (CW) images. (b, g) Lifetime maps from monoexponential fit; color bar indicates the lifetime in picoseconds. The decay amplitude distributions from a biexponential fit to the composite probe data are shown for Osteosense ($\tau_1 = 835$ ps) in (c, h) and for Kodak X-Sight 761 ($\tau_2 = 1343$ ps) in (d, i). (e, j) Merged amplitude distribution map shown as RGB images with amplitudes of Osteosense (blue) and X-Sight (red). (Reproduced from Raymond, S. B. et al., *Journal of Biomedical Optics* 15(4), 046011, 2010. With permission.)

of Kodak X-Sight results in a lifetime map with a large distribution of lifetimes, ranging from 1000 to 1500 ps (Figure 22.3g). Average lifetime at bony structures is significantly higher than with Osteosense alone, due to the contribution of vascular Kodak X-Sight. Biexponential fitting using average lifetimes for Osteosense ($\tau = 835$ ps) and Kodak X-Sight ($\tau = 1343$ ps) components results in clear anatomical separation of the two probes (Figure 22.3c–e, h–j). The Osteosense components before and after Kodak X-Sight administration are qualitatively similar (compare Figure 22.3c, h), and no Kodak X-Sight is detected by the biexponential fit before administration (Figure 22.3d).

22.3.5 NOISE CONSIDERATIONS FOR LIFETIME MULTIPLEXING

In the global analysis approach, we employ a linear fit with *a priori* lifetimes (estimated from separate measurements) to determine the amplitudes. The uncertainty (variance) in the decay amplitudes recovered from the linear fit, σ_{a_i} , depends on both the measurement noise and the separation ($\Delta\tau$) of the lifetimes involved. To estimate σ_{a_i} , we analyze the propagation of noise from the measurement (time domain image) to the recovered amplitudes using linear regression theory (Press et al. 1992). The time-dependent measurement, \mathbf{y} , is linearly related to the amplitudes of the individual decay components as $\mathbf{y} = X\mathbf{a}$, where the columns of X are normalized single-exponential decays, and \mathbf{a} are the component amplitudes. The uncertainty in the recovered amplitudes, σ_{a_i} , is dependent upon the measurement noise at each time point, expressed as a diagonal matrix Σ , where $\sum_{ii} = 1/\sigma_{y_i}^2$, and the respective basis functions X :

$$\sigma_{a_j}^2 = \left[\left(X^T \Sigma X \right)^{-1} \right]_{jj}. \quad (22.20)$$

Equation 22.20 allows calculation of recovered amplitude uncertainty given known system noise parameters (which determine Σ) and fluorophore lifetimes (which dictate the basis functions, X). Figure 22.4 shows the relative amplitude uncertainty (σ_{a_i}/a_i) simulated assuming a specific noise model for Σ relevant to a time-gated imaging system. It is seen that σ_{a_i}/a_i increases as the lifetime separation between probes, $\Delta\tau$, decreases (Figure 22.4a). For a given lifetime separation, the relative amplitude uncertainty for one component increases as the amplitude of the other component increases (Figure 22.4b). This means that if one component is much weaker than the other, it will have increased relative uncertainty. Fluorophore separability, defined arbitrarily as the conditions under which relative uncertainty is

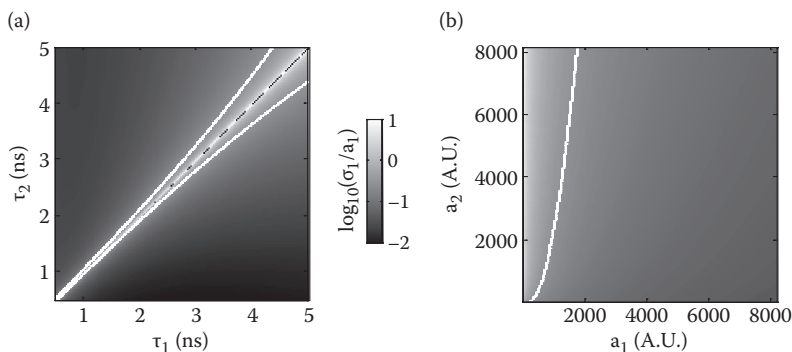


Figure 22.4 Influence of noise on the amplitude uncertainty for biexponential fits. Simulated biexponential fluorescence decays were generated for a noise model, $\sigma_y^2 = \beta y + \sigma_e^2$, with $\beta = 6.53$ and a dynamic range of 2^{14} (4×4 hardware and 2×2 software binning) for the time-gated intensifier camera (Kumar et al. 2008a). (a) Relative amplitude uncertainty for equal amplitude probes of varying lifetimes τ_1 and τ_2 . (b) Relative amplitude uncertainty of the first amplitude component for varying amplitudes, a_1 and a_2 , over the dynamic range of the instrument, with fixed lifetimes, $\tau_1 = 1$ ns, $\tau_2 = 1.2$ ns. The white lines in (a, b) indicate the 30% relative uncertainty contours. (Reproduced from Raymond, S. B. et al., *Journal of Biomedical Optics* 15(4), 046011, 2010. With permission.)

<30%, can be estimated directly as described above. For example, assuming one fluorophore with lifetime $\tau_1 = 1000$ ps, quantitative unmixing is possible for $\Delta\tau \geq 200$ ps at relative concentrations as low as 1:5 (Figure 22.4b). Measurement noise also affects the determination of the lifetime, τ , from a monoexponential fit, for example, when measuring the *in vivo* lifetime characteristics of a fluorophore. We estimated the propagation of measurement noise by simulating a fluorophore that has a fixed τ and realistic amplitude distribution (chosen from the mean lifetime and amplitude distribution of a similar *in vivo* measurement) and noise according to a conservative empirical model; the simulated measurement was then fit at each pixel for τ . As shown in Figure 22.5, the uncertainty in τ due to noise is $\approx 20\%$, which shows that a majority of the apparent *in vivo* lifetime heterogeneity is due to noise. This sets a limit on the number of fluorophores that may be multiplexed. Figure 22.6 shows the amplitude uncertainty with a simulation of lifetime multiplexing using up to five lifetimes using the shot noise model. This indicates that under the noise statistics used here, the maximum number of fluorophores that can be multiplexed reasonably (less than 30% relative amplitude uncertainty) is three.

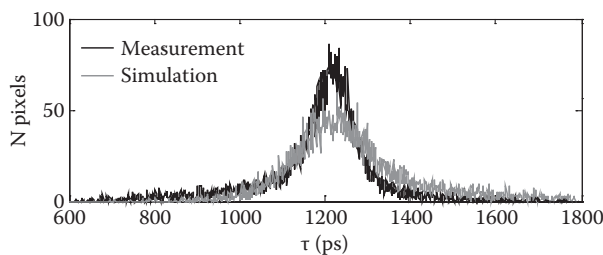


Figure 22.5 Influence of noise on lifetime uncertainty for monoexponential fits. The effects of measurement noise on estimation of τ for a single fluorophore were determined by simulating a measurement of Kodak X-Sight *in vivo*, using the mean lifetime and amplitude distribution of an actual Kodak X-Sight measurement. Noise was added according to an empirical noise model, $\sigma_y^2 = \beta y + \sigma^2$, with $\beta = 6.53$; each pixel was fit for τ and then plotted as a histogram. The measurement is shown above in black and the simulation in gray. The standard deviation for the measurement was 157 and the simulation was 193, which reflects the conservative noise model (adds slightly more noise than needed). (Reproduced from Raymond, S. B. et al., *Journal of Biomedical Optics* 15(4), 046011, 2010. With permission.)

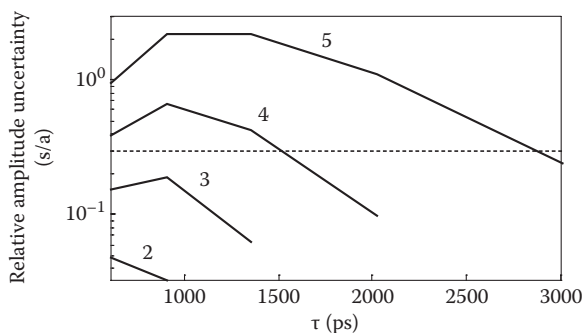


Figure 22.6 Amplitude uncertainty for multiple lifetime components was tested by simulating $n = 2-5$ lifetimes, with the initial lifetime $\tau_1 = 600$ ps and each additional lifetime $1.5\times$ the previous; amplitudes were split evenly between the components as $4096 \times 4/n$. Noise was added according to the conservative noise model for 4×4 hardware binning and 2×2 software binning. The relative uncertainty was calculated for each lifetime component as additional components were added. The 30% uncertainty cutoff is shown as a dotted line. (Reproduced from Raymond, S. B. et al., *Journal of Biomedical Optics* 15(4), 046011, 2010. With permission.)

22.4 IN VIVO TOMOGRAPHIC FLIM

As a demonstration of tomographic FLIM in living mice, we show lifetime multiplexing of Kodak X-Sight and Osteosense simultaneously injected in living nude mice ($n = 3$), using a time-resolved free-space tomographic imaging system (Kumar et al. 2008b; Raymond et al. 2010). Excitation and fluorescence measurements were collected 1 h after Kodak X-Sight administration from a grid (-3×3 mm separation) of 44 sources and ~ 100 detectors (Figure 22.7b). The asymptotic region was approximated as times t such that the quantity $\int_0^t e^{-t'/\tau} U_{exc} dt'$, where U_{exc} is the excitation measurement, approached 99% of its maximum value (Figure 22.4a; this is an experimental approximation for the quantity τ_D discussed in Section 22.2.4). The decays for all S–D pairs were fit in the asymptotic region for *a priori* lifetimes, $\tau_1 = 844$ ps and $\tau_2 = 1242$ ps, which were the mean *in vivo* lifetimes of X-sight and Osteosense injected separately in mice. Note that the scale for the Kodak X-Sight amplitude component is approximately fivefold greater than the Osteosense amplitude scale. The decay amplitudes for the two lifetimes at all S–D pairs (Figure 22.7f) were employed in Equation 22.8 to recover the full 3D yield distributions for Osteosense and X-sight. The 3D tomographic images shown in Figure 22.7g through j indicate that

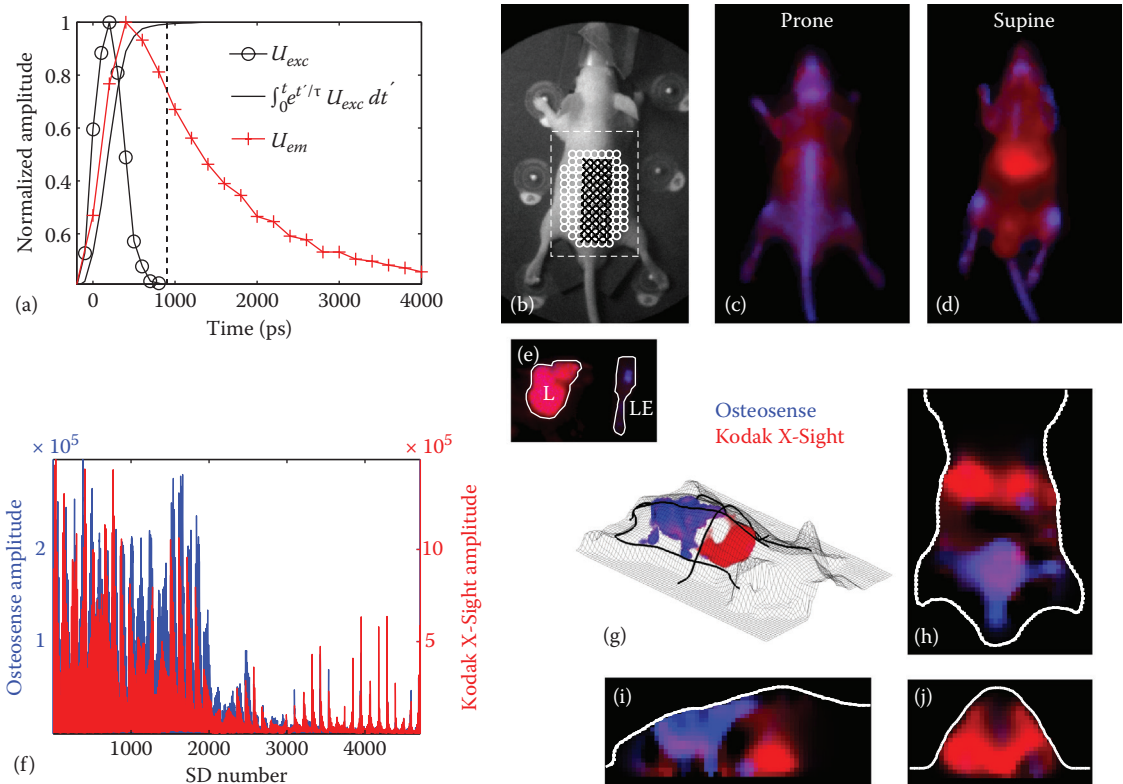


Figure 22.7 *In vivo* lifetime tomography of two anatomically targeted NIR fluorophores. Anesthetized nude mice were administered Osteosense (24 h prior) and Kodak X-Sight (1 h prior), and tomographic data were acquired for 44 sources and 107 detectors. Reconstructions used excitation (750/40 nm BP filter), emission (800 nm LP filter), and 3D-surface measurements using a 3D camera (Kumar et al. 2008b). (a) Representative time-resolved data for tomographic reconstructions. (b) Bright field image of with source (black “x”) and detector locations (white “o”). The reconstructed ROI is indicated with the dashed white rectangle. (c, d) Dual color, lifetime-unmixed, planar fluorescence images showing the amplitudes of Osteosense (blue) and Kodak X-Sight (red). (e) Postmortem organs (liver, L; amputated lower extremity, LE). (f) Recovered amplitude components for 44×107 SD pairs. (g) 3D rendering of surface (grid) and the Osteosense and Kodak X-Sight distributions. The location of slices in g–i are shown in bold black lines. (h–j) Slices from lifetime-separated reconstruction. Surface boundaries are indicated as solid white lines. (Reproduced from Raymond, S. B. et al., *Journal of Biomedical Optics* 15(4), 046011, 2010. With permission.)

Osteosense is confined to bony structures, including the spinal column, pelvis, skull, and long bones, whereas Kodak X-Sight has localized to the liver, with residual Kodak X-Sight in the vascular compartment (Figure 22.7c, d). These findings are consistent with the expected behavior of these two fluorophores and were confirmed by postmortem imaging of the organs and bones (Figure 22.7e). Thus, the tomographic-FLIM model separates and correctly localizes the spatial distribution of two lifetime components simultaneously present in a living animal.

22.5 CONCLUSIONS AND FUTURE OUTLOOK

In this chapter, we have presented theoretical and experimental methods for tomographic FLIM in turbid media. A forward model for TD fluorescence was presented that directly translates the multiexponential approach used in microscopic FLIM to 3D tomographic reconstructions in the whole body. The basis of this algorithm is the experimental observation that typical fluorophore lifetimes are longer than the intrinsic timescales for diffusive propagation of light through biological tissue and can therefore be directly measured from surface fluorescence decays. Further, we presented a rigorous formalism for isolating the individual 3D fluorescence yield distribution of each lifetime from a mixture of fluorophores using their tomographic surface decay amplitudes. Several commercial NIR fluorescent dyes are already available with capability for targeting specific disease pathologies in small animals. By a careful selection of dyes with lifetime contrast, the TD lifetime technology presented here will thus create new avenues to visualize multiple biological processes noninvasively, accelerating the drug discovery process in preclinical imaging, and can potentially offer interesting applications in the clinical settings as well.

The application areas for *in vivo* tomographic FLIM can be broadly classified into three categories based on contrast mechanism. The first is based on intrinsic contrast, for instance, the tracking of fluorescent protein (FP) labeled cancer cells or using intrinsic tissue autofluorescence (AF) to separate tissue types. FPs have revolutionized biological research (Giepmans et al. 2006) by allowing the visualization of cellular level processes using intravital microscopy. The ability to image FPs in whole animals will open several new avenues for monitoring biological processes in intact environments. However, a majority of existing FPs excite in the visible spectral range (400–600 nm), where tissue (AF) is significant. Previous attempts for imaging FPs in whole animals used CW techniques (Deliolani et al. 2008; Hoffman & Yang 2006), where the AF signal is indistinguishable from the FP fluorescence since it is intensity based. Recently, it has been shown that fluorescence lifetime allows improved detection of FPs against background tissue AF (Kumar et al. 2009; McCormack et al. 2007; Soloviev et al. 2007). Specially, the distinct nonexponential temporal response of AF decays as compared with the pure exponential decay of the fluorescence of several FPs *in vivo* has been used to enhance the imaging of GFP tumors in live mice (Kumar et al. 2009). The second application of preclinical whole-body lifetime imaging uses extrinsic fluorophores that are designed to undergo lifetime shifts *in vivo* due to a change in biochemical environment, such as pH (Berezin et al. 2011), protein binding (Goiffon et al. 2009), and binding to disease targets such as tumors (Bloch et al. 2005; Nothdurft et al. 2009).

Perhaps the most interesting and underexplored application of tomographic FLIM concerns activatable probes. For instance, Forster resonance energy transfer (FRET) probes have been widely used in FLIM (Vogel et al. 2006) and are based on nonradiative quenching of a pair of fluorophores located in close proximity (typically attached to a backbone such as a polymer) with overlapping absorption and emission spectra. Binding to a target enzyme or protein results in a conformational change or cleavage of the original pair, resulting in a dramatic increase in both fluorescence intensity and lifetime. While this mechanism has been explored for whole-body imaging using intensity-based CW techniques (Nahrendorf et al. 2007; Weissleder et al. 1999), lifetime-based applications of activatable probes are relatively recent (Goergen et al. 2012; McGinty et al. 2011; Solomon et al. 2011). Coupled with the fact that lifetime is a concentration- and intensity-independent functional marker of nonradiative quenching, this suggests that the future is bright for *in vivo* fluorescence lifetime tomography of activatable probes.

The central challenge for applying tomographic FLIM in the clinical setting (or whole-body human imaging) is the same as that for diffuse optical NIR spectroscopy, namely, the larger imaging volumes and the high absorption and scattering suffered by light photons in tissue. Although sophisticated algorithms

exist for modeling light transport through complex tissue, the limited penetration of diffuse light implies poor depth penetration and spatial resolution. However, recent advances in multimodality imaging have demonstrated the potential of NIR-diffuse optical tomography (DOT) for providing functional contrast in clinical applications (Fang et al. 2011). Tomographic FLIM can capitalize on these multimodal techniques since it relies on the same mathematical formalism as intrinsic contrast DOT. A second challenge for the clinical use of tomographic FLIM concerns the availability of disease-specific contrast agents and the subsequent long approval process for human use. With concurrent advances in lifetime-based targeted probe development (Berezin and Achilefu 2010), it is hoped that an increasing number of disease-specific fluorochromes will be available for human use, at which point tomographic FLIM is likely to play an important role in the clinical setting as well.

REFERENCES

- Arridge, S. (1999), 'Optical tomography in medical imaging,' *Inverse Problems* 15(2), R41–R93.
- Arridge, S. R. & Schotland, J. C. (2009), 'Optical tomography: Forward and inverse problems,' *Inverse Problems* 25(12), 123010.
- Barton, G. (1989), *Elements of Greens Functions and Propagation*. Oxford University Press, Oxford.
- Bastiaens, P. I. H. & Squire, A. (1999), 'Fluorescence lifetime imaging microscopy: Spatial resolution of biochemical processes in the cell,' *Trends in Cell Biology* 9(2), 48–52.
- Berezin, M. Y. & Achilefu, S. (2010), 'Fluorescence lifetime measurements and biological imaging,' *Chemical Reviews* 110(5), 2641–2684.
- Berezin, M. Y., Guo, K., Akers, W., Northdurft, R. E., Culver, J. P., Teng, B., Vasalatiy, O., Barbacow, K., Gandjbakhche, A., Griffiths, G. L. & Achilefu, S. (2011), 'Near-infrared fluorescence lifetime pH-sensitive probes,' *Biophysical Journal* 100(8), 2063–2072.
- Berezovska, O., Ramdya, P., Skoch, J., Wolfe, M. S., Bacskaï, B. J. & Hyman, B. T. (2003), 'Amyloid precursor protein associates with a nicastrin-dependent docking site on the presenilin 1-gamma-secretase complex in cells demonstrated by fluorescence lifetime imaging,' *Journal of Neuroscience*, 23(11), 4560–4566.
- Bertero, M. & Boccacci, P. (1998), *Introduction to Inverse Problems in Imaging*. Institute of Physics Publishing, London.
- Bloch, S., Lesage, F., McIntosh, L., Gandjbakhche, A., Liang, K. X. & Achilefu, S. (2005), 'Whole-body fluorescence lifetime imaging of a tumor-targeted near-infrared molecular probe in mice,' *Journal of Biomedical Optics* 10(5), 054003.
- Bremer, C., Ntziachristos, V. & Weissleder, R. (2003), 'Optical-based molecular imaging: Contrast agents and potential medical applications,' *European Radiology* 13(2), 231–243.
- Bugaj, J. E., Achilefu, S., Dorshow, R. B. & Rajagopalan, R. (2001), 'Novel fluorescent contrast agents for optical imaging of in vivo tumors based on a receptor-targeted dye-peptide conjugate platform,' *Journal of Biomedical Optics* 6(2), 122–133.
- Chandrasekhar, S. (1960), *Radiative Transfer*. Dover, New York.
- Deliolanis, N. C., Kasmieh, R., Würdinger, T., Tannous, B. A., Shah, K. & Ntziachristos, V. (2008), 'Performance of the red-shifted fluorescent proteins in deep-tissue molecular imaging applications,' *Journal of Biomedical Optics* 13(4), 044008.
- Durduran, T., Yodh, A. G., Chance, B. & Boas, D. A. (1997), 'Does the photon-diffusion coefficient depend on absorption?,' *Journal of the Optical Society of America A* 14, 3358–3365.
- Fang, Q., Selb, J., Carp, S. A., Boverman, G., Miller, E. L., Brooks, D. H., Moore, R. H., Kopans, D. B. & Boas, D. A. (2011), 'Combined optical and x-ray tomosynthesis breast imaging,' *Radiology* 258(1), 89–97.
- Giepmans, B. N. G., Adams, S. R., Ellisman, M. H. & Tsien, R. (2006), 'Review—The fluorescent toolbox for assessing protein location and function,' *Science* 312, 217–224.
- Goergen, C. J., Chen, H. H., Bogdanov, Jr., A., Sosnovik, D. E. & Kumar, A. T. N. (2012), 'In vivo fluorescence lifetime detection of an activatable probe in infarcted myocardium,' *Journal of Biomedical Optics* 17(5), 056001.
- Goiffon, R. J., Akers, W. J., Berezin, M. Y., Lee, H. & Achilefu, S. (2009), 'Dynamic noninvasive monitoring of renal function in vivo by fluorescence lifetime imaging,' *Journal of Biomedical Optics* 14, 020501.
- Hall, D., Ma, G., Lesage, F. & Yong, W. (2004), 'Simple time-domain optical method for estimating the depth and concentration of a fluorescent inclusion in a turbid medium,' *Optics Letters* 29(19), 2258–2260.
- Haselgrove, J. C., Schotland, J. C. & Leigh, J. S. (1992), 'Long-time behavior of photon diffusion in an absorbing medium: Application to time-resolved spectroscopy,' *Applied Optics* 31, 2678–2683.
- Hoffman, R. M. & Yang, M. (2006), 'Whole-body imaging with fluorescent proteins,' *Nature Protocols* 1(3), 1429–1438.
- Kumar, A. T. N., Chung, E., Raymond, S. B., van de Water, J., Shah, K., Fukumura, D., Jain, R. K., Bacskaï, B. J. & Boas, D. A. (2009), 'Feasibility of in vivo imaging of fluorescent proteins using lifetime contrast,' *Optics Letters* 34(13), 2066–2068.

- Kumar, A. T. N., Raymond, S. B., Bacskai, B. J. & Boas, D. A. (2008a), 'Comparison of frequency-domain and time-domain fluorescence lifetime tomography', *Optics Letters* 33(5), 470–472.
- Kumar, A. T. N., Raymond, S. B., Bacskai, B. J. & Boas, D. A. (2008b), 'A time domain fluorescence tomography system for small animal imaging', *IEEE Transactions on Medical Imaging* 27(8), 1152–1163.
- Kumar, A. T. N., Raymond, S. B., Boverman, G., Boas, D. A. & Bacskai, B. J. (2006), 'Time resolved fluorescence tomography of turbid media based on lifetime contrast', *Optics Express* 14(25), 12255–12270.
- Kumar, A. T. N., Skoch, J., Bacskai, B. J., Boas, D. A. & Dunn, A. K. (2005), 'Fluorescence-lifetime-based tomography for turbid media', *Optics Letters* 30(24), 3347–3349.
- Kumar, A., Zhu, L., Christian, J., Demidov, A. & Champion, P. M. (2001), 'On the rate distribution analysis of kinetic data using the maximum entropy method: Applications to myoglobin relaxation on the nanosecond and femtosecond timescales', *Journal of Physical Chemistry B* 105, 7847–7856.
- Massoud, T. & Gambhir, S. (2003), 'Molecular imaging in living subjects: Seeing fundamental biological processes in a new light', *Genes & Development* 17(5), 545–580.
- Matthews, J. & Walker, R. (1970), *Mathematical Methods of Physics*, 2nd ed. Addison-Wesley, Reading, MA.
- McCormack, E., Micklem, D. R., Pindard, L. E., Silden, E., Gallant, P., Belenkov, A., Lorens, J. B. & Gjertsen, B. T. (2007), 'In vivo optical imaging of acute myeloid leukemia by green fluorescent protein: Time-domain autofluorescence decoupling, fluorophore quantification, and localization', *Molecular Imaging* 6(3), 193–204.
- McGinty, J., Stuckey, D. W., Soloviev, V. Y., Laine, R., Wylezinska-Arridge, M., Wells, D. J., Arridge, S. R., French, P. M. W., Hajnal, J. V. & Sardini, A. (2011), 'In vivo fluorescence lifetime tomography of a FRET probe expressed in mouse', *Biomedical Optics Express* 2(7), 1907–1917.
- Milstein, A. B., Oh, S., Webb, K. J., Bouman, C. A., Zhang, Q., Boas, D. A. & Millane, R. P. (2003), 'Fluorescence optical diffusion tomography', *Applied Optics* 42(16), 3081–3094.
- Milstein, A. B., Stott, J. J., Oh, S., Boas, D. A., Millane, R. P., Bouman, C. A. & Webb, K. J. (2004), 'Fluorescence optical diffusion tomography using multiple-frequency data', *Journal of the Optical Society of America A-Optics Image Science and Vision* 21(6), 1035–1049.
- Nahrendorf, M., Sosnovik, D. E., Waterman, P., Swirski, F. K., Pande, A. N., Aikawa, E., Figueiredo, J. L., Pittet, M. J. & Weissleder, R. (2007), 'Dual channel optical tomographic imaging of leukocyte recruitment and protease activity in the healing myocardial infarct', *Circulation Research* 100(8), 1218–1225.
- Niedre, M. J., de Kleine, R. H., Aikawa, E., Kirsch, D. G., Weissleder, R. & Ntziachristos, V. (2008), 'Early photon tomography allows fluorescence detection of lung carcinomas and disease progression in mice in vivo', *Proceedings of the National Academy of Sciences of the United States of America* 105(49), 19126–19131.
- Nothdurft, R. E., Patwardhan, S. V., Akers, W., Ye, Y. P., Achilefu, S. & Culver, J. P. (2009), 'In vivo fluorescence lifetime tomography', *Journal of Biomedical Optics* 14(2), 024004.
- Patterson, M. S., Chance, B. & Wilson, B. C. (1989), 'Time-resolved reflectance and transmittance for the non-invasive measurement of tissue optical properties', *Applied Optics* 28, 2331–2336.
- Press, W. H., Flannery, B. P., Teukolsky, S. A. & Vetterling, W. T. (1992), *Numerical Recipes in C: The Art of Scientific Computing*, 2nd ed. Cambridge University Press, New York.
- Raymond, S. B., Boas, D. A., Bacskai, B. J. & Kumar, A. T. N. (2010), 'Lifetime-based tomographic multiplexing', *Journal of Biomedical Optics* 15(4), 046011.
- Selvin, P. R. (2000), 'The renaissance of fluorescence resonance energy transfer', *Nature Structural Biology* 7(9), 730–734.
- Solomon, M., Guo, K., Sudlow, G. P., Berezin, M. Y., Edwards, W. B., Achilefu, S. & Akers, W. J. (2011), 'Detection of enzyme activity in orthotopic murine breast cancer by fluorescence lifetime imaging using a fluorescence resonance energy transfer-based molecular probe', *Journal of Biomedical Optics* 16(6), 066019.
- Soloviev, V. Y., McGinty, J., Tahir, K. B., Neil, M. A. A., Sardini, A., Hajnal, J. V., Arridge, S. R. & French, P. M. W. (2007), 'Fluorescence lifetime tomography of live cells expressing enhanced green fluorescent protein embedded in a scattering medium exhibiting background autofluorescence', *Optics Letters* 32(14), 2034–2036.
- Vogel, S., Thaler, C. & Koushik, S. V. (2006), 'Fanciful fret', *Science's STKE: Signal Transduction Knowledge Environment*, 2006(331), re2.
- Weissleder, R., Tung, C. H., Mahmood, U. & Bogdanov, A. (1999), 'In vivo imaging of tumors with protease-activated near-infrared fluorescent probes', *Nature Biotechnology* 17(4), 375–378.